

# Pose Measurement at Small Scale by Spectral Analysis of Periodic Patterns

Antoine N. André, Patrick Sandoz\*, Maxime Jacquot, Guillaume J. Laurent

## Abstract

The retrieval of an observed object's pose is an essential computer vision problem. The challenge arises in many different fields, among them robotics control, contactless metrology, or augmented reality. When the observed object shrinks from the macroscopic scale to the microscopic, pose estimation is further complicated by the weaker perspective of imaging macroscale lenses down to the quasi-orthographic projection inherent to microscope objectives. This paper tackles this issue of microscale pose estimation in two complementary steps that rely on the use of planar periodic targets. We first consider the orthographic projection case as a means of presenting the theory of the method and showing how the pose of periodic patterns can be directly retrieved from the Fourier frequency spectrum of a given image. We then address the perspective case with long focal lengths, in which the full six-degrees of freedom (6-DOF) pose can be retrieved without ambiguities by following the same theoretical background. In addition to theoretically justifying pose retrieval via Fourier analysis of acquired images, this paper demonstrates the method's actual performance. Both simulations and experimentation are conducted to validate the method and confirm an experimental resolution lower than  $1/1000^{th}$  of a pixel for translations. For orientation measurement, resolutions below  $1 \mu\text{rad}$ . for in-plane orientation, and below  $100 \mu\text{rad}$ . for off-axis orientations can be achieved.

## Index Terms

Fiducial markers, Fourier analysis, pose measurement

## I. INTRODUCTION

Pose measurement is a classic computer vision problem whose applications can be found in various fields, including robotics control, contactless metrology or augmented reality. Some methods rely on the use of multiple cameras to reconstruct the object and its pose via well-known feature matching techniques such as SIFT or SURF (Bay et al., 2006; Moreels and Perona, 2007). Other proposed methods rely on just one camera, using properties of the scene to retrieve the observed object's coordinates in the camera frame referential.

This problem of single camera pose estimation has already been widely researched, and many different techniques have been investigated by exploiting various hypotheses or constraints, including the rigidity of observed objects, the coplanarity of studied points, and the use of different kinds of camera projection models. Tamadazte et al. (2010) and Drummond and Cipolla (2002), for example, both tackled the problem in their attempt to retrieve complex objects' poses for visual tracking. Loing et al. (2018) also explored the problem in the realm of robotics, proposing a method of retrieving the relative pose between a robot and an object with the aid of neural networks.

One widely spread approach to single-camera pose estimation is to search for features that are physically constrained in the same plane. For example, with checkerboard patterns, this method can be used for both calibration and pose estimation, as described by Liu et al. (2016); Bouguet (2004). These features can also be organized more compactly so as to create fiducial markers that are present in the field of pose estimation for a several decades, as described by Kato and Billinghurst (1999), who envisioned applications in the realm of augmented reality. In the decades since Bruckstein et al. (1999) proposed novel designs for fiducial markers that would lie on a single plane for pose estimation and explored innovative markers Bruckstein et al. (2000). Many more designs have been explored, notably by Fiala (2005), Sattar et al. (2007), and Naimark and Foxlin (2002). Among these, ARTags and ArUco markers (Garrido-Jurado et al., 2014) are perhaps the most popular, having quickly become the bases of numerous applications. Indeed, such applications are not only numerous, but also quite varied, ranging from macroscopic scale applications with excavators pose estimation as shown by Azar et al. (2015) to microscopic scale with MEMS pose retrieval as described by Kim et al. (2015). As the design of fiducial markers evolved, so too did methods for their pose estimation, and recent works by Didier et al. (2008), Collins and Bartoli (2014) or Zhong and Zhang (2019) detail higher resolution and more robust measures.

However, as size of the observed object decreases, the focal length of the lens must increase accordingly. This has led a new challenge in pose measurement to emerge as the perspective projection on the camera becomes weaker. As recently observed by Yao et al. (2021) in a survey of different pose measurement techniques in the microscopy field, this change in the scale at which measurement occurs raises newly complicates process of retrieving the pose of an observed object.

\*Corresponding author

The authors are with the FEMTO-ST Institute, Univ. Bourgogne Franche-Comté, UMR CNRS 6174, 25000 Besançon, France

### A. Contributions

This article proposes a novel method: retrieving a pose from an observed periodic pattern within the Fourier domain by extending the high-resolution in-plane measure provided by periodic patterns to a six-degrees of freedom (6-DOF) pose measure. Assuming that one is working with an orthographic projection, a 5-DOF pose and accompanying scale factor can be measured; considering a perspective projection with a long focal length, an unambiguous 6-DOF pose can be obtained by extending the scale factor measure to the depth measure. This article proposes a formal method of extracting from the Fourier domain all the information needed to retrieve a 6-DOF pose of bi-dimensional periodic patterns.

Alongside with the methodology of pose measurement, this article presents the performances of the measure by simulations with generated images and confronting these results with experimental validations. Finally, this article compares the presented method in simulation with the 6-DOF pose estimation of circular grids for a set of four different projection configurations and its experimental performances with other fiducial markers (AruCo tags, checkerboard).

### B. Paper structure

The article is organized into five main sections which together present the method of pose measurement and detail its performance. Section II outlines the phase-based background for in-plane pose measurement; section III tackles the theoretical problem of pose determination with the help of a periodic pattern observed under orthographic projection by presenting the method of retrieving the 5-DOF and scale factor in the Fourier domain. Section IV expands this measure to a sixth degree of freedom by considering a perspective projection with a long focal length that allows the retrieval of the depth measure. Then, in section V the validity of the method and its range of measure are demonstrated with simulated periodic patterns poses. Section VI presents the experimental validation of the results both with a microscope objective and with a macro objective to confirm that the measure is valid across different projections. Finally, section VII ends the papers by defining directions of future work.

## II. RELATED AND PREVIOUS WORKS

### A. Pose measurement in microscopy

Even when the pose can only be measured along 3-DOF, pose estimation problem at small scale remains relevant for as diverse domains as biology or micro-robotics. For this reason, different methods of in-plane pose sensing have been studied in recent years. These methods can be grouped in three main categories. The first class uses features present in the image to recover the  $x, y, \alpha$  pose of the observed object; this category of method is presented in previous research by Chu et al. (2012), Liu et al. (2013), and Shang et al. (2016). The approach has its limits: if only the position of groups of pixels is studied, the best achievable resolution is only one tenth of a pixel. Correlation methods, in contrast, have demonstrated superior resolutions. By studying the faint pixel changes between one image and another to retrieve the in-plane pose, a resolution as fine as one hundredth of a pixel can be attained, as shown by Marturi et al. (2016), Bomarito et al. (2017), and Li et al. (2019). To achieve even better resolutions, periodic patterns can be printed on the surface of observed objects. The redundancy of this grating in combination with the phase evolution of the pattern, leads to resolutions as high as a thousandth of a pixel. This method has already proven its capabilities in term of resolution performance and large range of measure (Kim et al., 2018; Guelpa et al., 2014). The method of pose measurement presented in this article leans on the previously studied in-plane pose measurement technique (Andre et al., 2020) and extends it to a full 6-DOF pose measure that retains high resolution.

### B. In-plane pose measurement in Fourier domain

Analysis of the phase tied to a periodic pattern is a known, convenient way of measuring the in-plane position and subsequent displacements of a target observed by a vision system. This method has been largely used with one dimensional periodic gratings in different researches and with different approaches such as classic phase studying, Moiré fringe studying or Vernier phase studying, as described by Yamahata et al. (2010), Ri et al. (2014), Sugiura et al. (2015), and Guelpa et al. (2014). The main advantage of these methods is the high-resolution sub-pixel measure that can be achieved via the phase analysis of the periodic grating along one axis.

This periodic pattern designs can be extended into two dimensions, thereby generating a high-resolution in-plane measure along the three coordinates  $(x, y, \alpha)$ . The 2D Fourier transform of such pattern is presented in Fig. 1. Its periodic arrangement results in four main peaks in the Fourier domain. The link between the frequency domain and the spatial one can be described as follow:

$$\begin{cases} x = \frac{\varphi_1}{2\pi}\lambda + k_1\lambda \\ y = \frac{\varphi_2}{2\pi}\lambda + k_2\lambda \\ \alpha = \text{atan2}(n_1, m_1) + k_3\frac{\pi}{2} \end{cases} \quad (1)$$

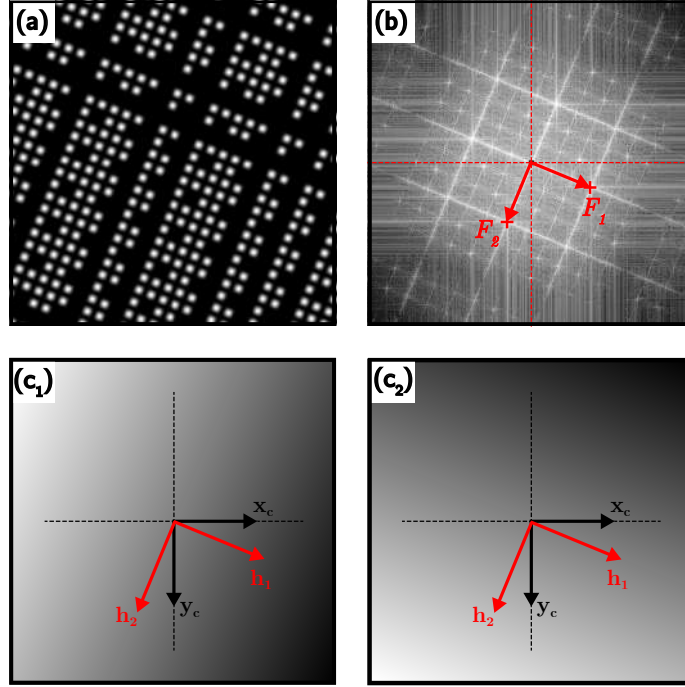


Fig. 1: In-plane pose measurement process with (a) an image of a pseudo-periodic encoded pattern, (b) the corresponding spectrum of the pattern image resulting from the Fourier transform, (c<sub>1</sub>) the inverse Fourier transform phase evolution along the first direction and (c<sub>2</sub>) along the second direction once  $2\pi$  unwrapped. Vectors  $\mathbf{h}_1$  and  $\mathbf{h}_2$  denote the main direction vectors associated with each phase plane

where  $\varphi_1$  and  $\varphi_2$  are the phase values of peaks  $F_1$  and  $F_2$ ,  $\lambda$  is the physical period of the pattern.  $k_1$  and  $k_2$  stand for the unknown orders of the lines and columns of dots with respect to the whole pattern design and allowing to switch from a relative pose measurement to an absolute one. Angle measurement is made by using the peak position  $F_1$  whose coordinates are  $[m_1, n_1]^T$  in the Fourier domain and  $k_3$  is the quadrant number of the imaged periodic pattern.

This method has been notably explored in previous articles such as Sandoz et al. (2002) or Chen and Huang (2016) to perform highly resolute in-plane pose measurement. However the main drawback of this highly resolute method is its range of measure which is limited to one period. To extend this range of measure, a binary sequence can be encrypted within the periodic pattern, thus ensuring absolute in-plane pose sensing through the unambiguous identification of the period orders  $k_1$ ,  $k_2$  and the quadrant number  $k_3$  of every imaged area of the pattern.

### C. Absolute in-plane pose measurement

Different methods of inserting binary code in periodic patterns for absolute pose registration have been explored, notably by Kim et al. (2018) or Andre et al. (2020). This paper relies on the pseudo-periodic pattern design proposed by the latter which is built according to the following steps. First, a bi-dimensional periodic grating of physical period  $\lambda$  is created. Then, a linear feedback shift register binary sequence is added to the pattern such that distortions of the periodic frame phase are avoided and, by padding with neutral lines and columns, a sufficient magnitude is retained for the spatial frequency of interest. Finally, rotation keying is added to allow for an absolute angle determination over  $2\pi$  by removing specific dots in the pattern (the resulting pattern is depicted in Fig. 1.(a)). This encoding method can easily be scaled, making possible various resolutions and ranges of measure, as shown in previous works (André et al., 2020).

This pseudo-periodic pattern embeds two kinds of information: the first relies on the periodicity of the dots, which allows fine pose measurement based on the phase analysis of the pattern, and the second allows absolute position retrieval over a large range as well as absolute angle measurement based on the pattern's binary decoding. This decoding step involves the application of a local threshold to different phase maps of the pattern leading to the retrieval of the fringe counts  $k_1$ ,  $k_2$  and quadrant number  $k_3$ . In this fashion, an absolute and unambiguous pose measurement with a high sub-pixel resolution can be achieved for the in-plane case, and the measurement shows great robustness across different image alterations (André et al., 2021).

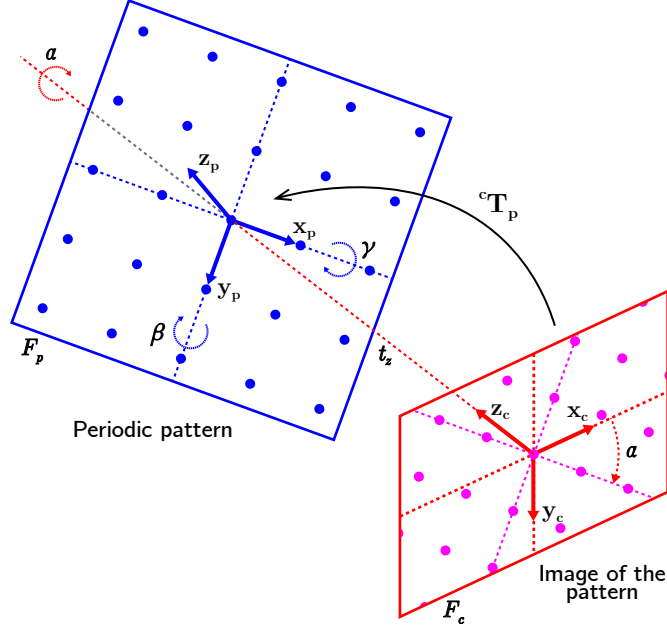


Fig. 2: 3D view of the orthographic projection of the pattern on the image with referential convention annotated

This article extends this in-plane pose determination method to a full 6-DOF pose measurement through a deeper analysis of the spectral phase in the Fourier domain. Both the orthographic case and the perspective case with long focal lengths are separately examined, and the theory of the method is presented alongside its validation, which is demonstrated by both simulations and experiments.

### III. 5-DOF POSE MEASUREMENT METHOD UNDER ORTHOGRAPHIC PROJECTION

#### A. Referential conventions and notations

As the method detailed in this paper is based on studying periodic patterns in the spectral domain by examining the frequency peaks that embed the pose information, an orthographic projection is considered to conduct the theoretical calculus. This projection allows the conservation of physical periods' proportions in the image and therefore produces punctual peaks ( $F_1$  and  $F_2$  as presented in Fig. 3.(b)) in the Fourier spectrum, which contains all information necessary to measure 6-DOF: the  $x, y$  translations, the  $\alpha, \beta, \gamma$  orientations and the scale factor  $s$  of the pattern pose. Indeed, both peaks  $F_1$  and  $F_2$  of the Fourier transform carry their location  $[m_1, n_1]^T$ ,  $[m_2, n_2]^T$  and the phase value at the peak  $\varphi_1, \varphi_2$ .

Before considering how the spectrum of the image can be processed to retrieve the 6-DOF, the principal properties of this projection convention must be covered. Let us begin by defining the (scaled) dhorthographic projection:

$$\begin{bmatrix} u \\ v \\ 1 \end{bmatrix} = \begin{bmatrix} s & 0 & 0 & 0 \\ 0 & s & 0 & 0 \\ 0 & 0 & 0 & 1 \end{bmatrix} \cdot {}^c\mathbf{T}_p \cdot \begin{bmatrix} P_x \\ P_y \\ P_z \\ 1 \end{bmatrix} \quad (2)$$

where  $[u, v]^T$  is the projected point on the image sensor of the observed point  $[P_x, P_y, P_z]^T$  in the object frame and where  $s$  is the unknown millimeter-to-pixel factor.  ${}^c\mathbf{T}_p$  is the transformation matrix representing the pose of the frame of the pattern in the image sensor referential. Fig. 2 presents both referentials  $\mathcal{F}_c$  (frame attached to the camera) and  $\mathcal{F}_p$  (frame attached to the observed pattern) with the  ${}^c\mathbf{T}_p$  transformation between them. By considering these successive measurement steps, the transformation matrix between the periodic pattern and the image of the pattern can be defined as follows:

$${}^c\mathbf{T}_p = \text{transl}(0, 0, z) \cdot \text{rotz}(\alpha) \cdot \text{roty}(\beta) \cdot \text{rotx}(\gamma) \cdot \text{transl}(x, y, 0) \quad (3)$$

$\alpha, \beta$  and  $\gamma$  are the Tait-Bryan angles describing the object's orientation. This form of transformation has been chosen to ease the calculation of off-axis angles, as it will be demonstrated in the following explanations of the method.

### B. In-plane pose measurement

As outlined in section II, the pose measurement relies on the study of the phase of the observed pattern, which is obtained by taking advantage of the shifted 2D Fourier transform of the acquired pattern image. This transformation of an image from spatial domain to frequency domain can be expressed as follows:

$$\hat{\mathbf{I}}(m, n) = \sum_{u=0}^w \sum_{v=0}^h \mathbf{I}(u, v) \cdot e^{-2\pi i \left[ \left( \frac{u}{w} - \frac{1}{2} \right) m + \left( \frac{v}{h} - \frac{1}{2} \right) n \right]} \quad (4)$$

where  $\mathbf{I}$  is the pixel value of the acquired image and  $w$  and  $h$  are respectively the width and the height of the image. The resulting projection of a periodic pattern and its discrete Fourier transform can also be seen in Fig. 3.(a). The periodicity of the target results in four main peaks in the Fourier spectrum, with symmetrical peaks being complex conjugates of each other. These peaks in the Fourier domain are depicted in Fig. 3.(b). By studying the position  $[m_1, n_1]$ ,  $[m_2, n_2]$  and the phase  $\varphi_1$ ,  $\varphi_2$  of these peaks, the  $[x, y, \alpha, \beta, \gamma]^T$  pose of the pattern can be measured, along with the scale factor  $s$ .

To increase the resolution of the phase measurements and the peak locations despite the discrete form of the Fourier transform, two phase maps of the pattern are computed back in the spatial domain using the following process. The coordinates of the two main frequency peaks representative of each direction of the periodic pattern are first retrieved (as depicted in Fig. 1.(b)). This step is made by searching for the pixels of highest modulus. In order to avoid phase distortion due to spectrum discretization, the inverse Fourier transform is computed for each frequency peaks  $F_1$  and  $F_2$  after the application of a Gaussian filter mask on each frequency peak respectively. This step therefore insures the conservation of all the peak information (and by extension the phase information) when doing the inverse Fourier transform. A better phase understanding of the periodic pattern can be done by unwrapping the two phase images resulting from the inverse Fourier transform as shown in Fig. 1.(c<sub>1</sub>), (c<sub>2</sub>).

These two phase maps encode the position of the pattern features with respect to the image pixel frame with a high resolution. The two phase maps evolution can be expressed by means of regression plane:

$$\Phi_i(u, v) = a_i u + b_i v + c_i \quad (5)$$

where  $i$  is 1 or 2 to denote the main directions of the pattern. The constant  $c_i$  gives a highly resolute measure of the phase of the peak  $i$ :

$$\varphi_i = c_i \quad (6)$$

The position of the two main frequency peaks can be retrieved from the two phase planes equation:

$$\begin{cases} m_i = \frac{w \cdot a_i}{2\pi} \\ n_i = \frac{h \cdot b_i}{2\pi} \end{cases} \quad (7)$$

Another link between the phase plane equations and the spatial coordinates of the pattern referential can be expressed, based on the fact that each of the points constituting the referential is  $2\pi$  farther from the center of the pattern image. Thus, the main director vectors of the phase evolution along each direction  $\mathbf{h}_1 = [u_1, v_1]^T$  and  $\mathbf{h}_2 = [u_2, v_2]^T$  that can be seen in Fig. 1.(c<sub>1</sub>), (c<sub>2</sub>), are expressed by:

$$\begin{cases} u_1 = \frac{b_1 \cdot c_2 - (c_1 - 2\pi) \cdot b_2}{a_1 \cdot b_2 - a_2 \cdot b_1} \\ v_1 = \frac{a_2 \cdot (c_1 - 2\pi) - a_1 \cdot c_2}{a_1 \cdot b_2 - a_2 \cdot b_1} \end{cases} \quad (8)$$

and

$$\begin{cases} u_2 = \frac{b_1 \cdot (c_2 - 2\pi) - c_1 \cdot b_2}{a_1 \cdot b_2 - a_2 \cdot b_1} \\ v_2 = \frac{a_2 \cdot c_1 - a_1 \cdot (c_2 - 2\pi)}{a_1 \cdot b_2 - a_2 \cdot b_1} \end{cases} \quad (9)$$

To measure the pose, the  $(x, y)$  position in the pattern referential is processed first. Then, the pattern orientation  $\alpha$  is computed accordingly to Eq. (1). Finally, the two off-axis angles  $(\beta, \gamma)$  are measured according to the method explained in the following. The distance between the pattern and the image  $z$  is excluded as it cannot be determined with an orthographic projection. The scale factor  $s$  of the projection, however, can be measured; it corresponds to a sixth DOF which will be converted into  $z$ -information in the perspective case.

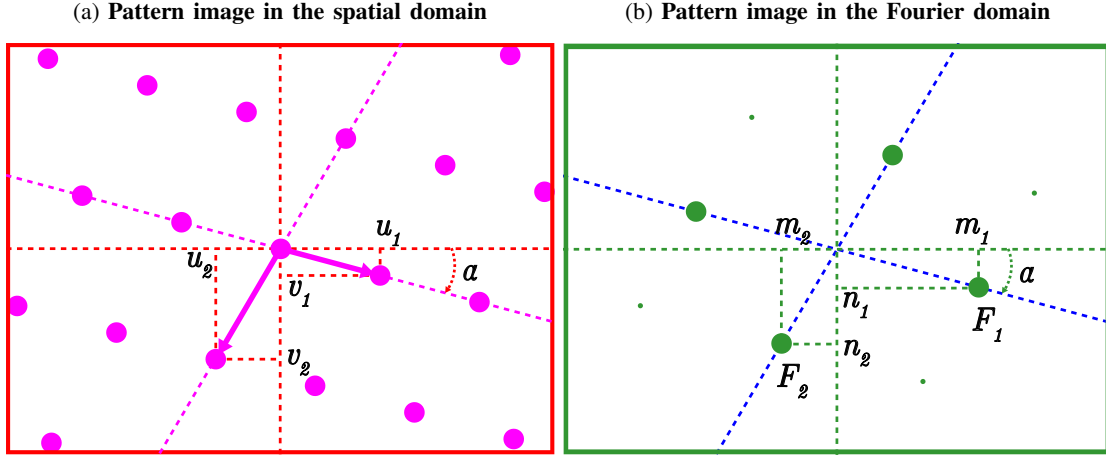


Fig. 3: (a) Front view of the orthographic projection of the pattern on the image sensor and (b) Main lobes of the Fourier transform of the periodic pattern with main periodic peaks  $F_1$  at  $[m_1, n_1]^T$  and  $F_2$  at  $[m_2, n_2]^T$

### C. Off-axis angles measurement

To recover the two off-axis angles of the observed pattern pose, along with the scale factor, the peaks' coordinates in the spectral domain are used. Indeed, these two vectors are directly linked with the two unit vectors defining the pattern referential as explained in previous section (with image coordinates  $\mathbf{h}_1 = [u_1, v_1]^T$  and  $\mathbf{h}_2 = [u_2, v_2]^T$ , as shown in Fig. 3.(a) sizing one period long  $\lambda \mathbf{x}_p = [\lambda, 0, 0]^T$  and  $\lambda \mathbf{y}_p = [0, \lambda, 0]^T$ .

By projecting these two points from the pattern frame to the image frame with the projection matrix  ${}^c\mathbf{T}_p$ , a link between the pattern angles and the pattern direction vectors can be established:

$$\begin{bmatrix} u_1 \\ v_1 \\ 1 \end{bmatrix} = \begin{bmatrix} s & 0 & 0 & 0 \\ 0 & s & 0 & 0 \\ 0 & 0 & 0 & 1 \end{bmatrix} \cdot {}^c\mathbf{T}_p \cdot \begin{bmatrix} \lambda \\ 0 \\ 0 \\ 1 \end{bmatrix} = s\lambda \begin{bmatrix} \cos \alpha \cos \beta \\ \sin \alpha \cos \beta \\ 1 \end{bmatrix} \quad (10)$$

The projection of the second direction vector  $\lambda \mathbf{y}_p = [0; \lambda; 0]$  gives:

$$\begin{bmatrix} u_2 \\ v_2 \\ 1 \end{bmatrix} = \begin{bmatrix} s & 0 & 0 & 0 \\ 0 & s & 0 & 0 \\ 0 & 0 & 0 & 1 \end{bmatrix} \cdot {}^c\mathbf{T}_p \cdot \begin{bmatrix} 0 \\ \lambda \\ 0 \\ 1 \end{bmatrix} \quad (11)$$

giving

$$\begin{aligned} \begin{bmatrix} u_2 \\ v_2 \end{bmatrix} &= s\lambda \begin{bmatrix} \cos \alpha \sin \beta \sin \gamma - \sin \alpha \cos \gamma \\ \sin \alpha \sin \beta \sin \gamma + \cos \alpha \cos \gamma \end{bmatrix} \\ &= s\lambda \begin{bmatrix} \cos \alpha & -\sin \alpha \\ \sin \alpha & \cos \alpha \end{bmatrix} \begin{bmatrix} \sin \beta \sin \gamma \\ \cos \gamma \end{bmatrix} \end{aligned} \quad (12)$$

Which can be rearranged in:

$$\begin{bmatrix} \cos \alpha & \sin \alpha \\ -\sin \alpha & \cos \alpha \end{bmatrix} \cdot \begin{bmatrix} u_2 \\ v_2 \end{bmatrix} = s\lambda \begin{bmatrix} \sin \beta \sin \gamma \\ \cos \gamma \end{bmatrix} \quad (13)$$

Peaks coordinates in the Fourier spectrum give:

$$\begin{aligned} u_1^2 + v_1^2 &= s^2 \lambda^2 (\cos^2 \alpha \cos^2 \beta + \sin^2 \alpha \cos^2 \beta) \\ &= s^2 \lambda^2 \cos^2 \beta \end{aligned} \quad (14)$$

Thus:

$$\cos^2 \beta = \frac{u_1^2 + v_1^2}{s^2 \lambda^2} = \frac{b}{s^2} \quad \text{with } b = \frac{u_1^2 + v_1^2}{\lambda^2} \quad (15)$$

Similarly, from equation 13, we have:

$$\begin{aligned} \cos^2 \gamma &= \frac{(-u_2 \sin \alpha + v_2 \cos \alpha)^2}{s^2 \lambda^2} = \frac{g}{s^2} \\ \text{with } g &= \frac{(-u_2 \sin \alpha + v_2 \cos \alpha)^2}{\lambda^2} \end{aligned} \quad (16)$$

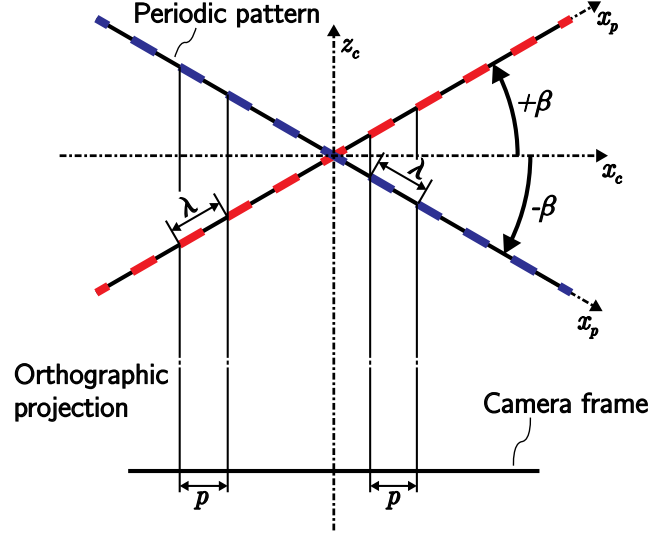


Fig. 4: Same periodic pattern of period  $\lambda$  rotated of  $+\beta$  (in red) and  $-\beta$  (in blue) and imaged via an orthographic projection on a camera frame, resulting in the same perceived pixelic period  $p$

and

$$\sin^2 \beta \sin^2 \gamma = \frac{(u_2 \cos \alpha + v_2 \sin \alpha)^2}{s^2 \lambda^2} = \frac{d}{s^2} \quad (17)$$

with  $d = \frac{(u_2 \cos \alpha + v_2 \sin \alpha)^2}{\lambda^2}$

giving:

$$(1 - \cos^2 \beta) (1 - \cos^2 \gamma) = \frac{d}{s^2} \quad (18)$$

By replacing  $\cos^2 \beta$  and  $\cos^2 \gamma$  in the equation above, a second order equation for determining  $s$  is then deduced:

$$s^4 - (b + g + d)s^2 + bg = 0 \quad (19)$$

As  $s$  is positive, two solutions are found:

$$s_1 = \sqrt{\frac{(b + g + d) + \sqrt{(b + g + d)^2 - 4bg}}{2}} \quad (20)$$

$$s_2 = \sqrt{\frac{(b + g + d) - \sqrt{(b + g + d)^2 - 4bg}}{2}} \quad (21)$$

By solving these equations, two groups of 4 symmetric solutions for  $\beta$  and  $\gamma$  can be deduced from eq. 15 and eq. 16:

$$\begin{cases} \beta_1 = \pm \cos^{-1} \left( \frac{\sqrt{b}}{s_1} \right) \\ \gamma_1 = \pm \cos^{-1} \left( \frac{\sqrt{g}}{s_1} \right) \end{cases} \quad \text{and} \quad \begin{cases} \beta_2 = \pm \cos^{-1} \left( \frac{\sqrt{b}}{s_2} \right) \\ \gamma_2 = \pm \cos^{-1} \left( \frac{\sqrt{g}}{s_2} \right) \end{cases} \quad (22)$$

#### D. Reduced set of solutions

Among this set of solutions, some of them can be removed, as it is the case for the solutions given by the second scale factor  $s_2$ . Since  $\frac{\sqrt{b}}{s_2} > 1$ , solutions given by this set would lead to an evaluation of an arc-cosine larger than one. Setting aside the solutions for  $\beta_2$  and  $\gamma_2$ , a more comprehensive understanding of the remaining solutions can be studied. However, owing to the parallel-ray structure inherent in the orthographic projection, it is impossible to remove the  $\pm$  ambiguity from the remaining solution for  $\beta_1$  and  $\gamma_1$ .

Fig. 4 presents a more visual way of understanding this ambiguity in the  $\beta$  and  $\gamma$  solutions with a periodic pattern rotating around the  $\beta$  axis (positively in red and negatively in blue), imaged via an orthographic projection on the camera plane. As the periodic pattern rotates from the same angle, either positively (as denoted by  $+\beta$ ) or negatively (denoted by  $-\beta$ ), the physical period  $\lambda$  results in the same imaged period  $p$  on the camera frame. This same ambiguity similarly affects the  $\gamma$  orientation.

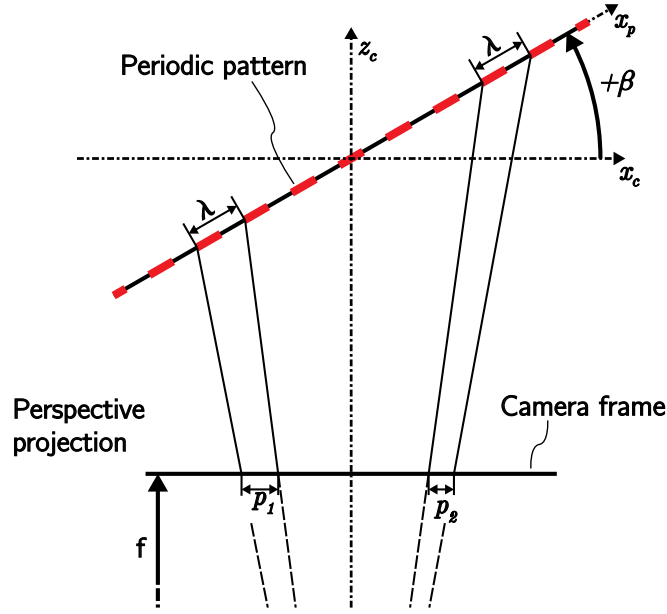


Fig. 5: Perspective projection of a rotated periodic pattern presenting different imaged pixelic period, depending of the distance of the pattern to the camera frame

With this ambiguity in the angle determination in mind and the solutions derived from the second scale factor  $s_2$  set aside, the final solution for off-axis angles  $\beta$  and  $\gamma$  can be written as follows:

$$\left\{ \begin{array}{l} \beta_1 = \cos^{-1} \left( \frac{\sqrt{b}}{s_1} \right) ; \quad \gamma_1 = \cos^{-1} \left( \frac{\sqrt{g}}{s_1} \right) \\ \beta_2 = -\cos^{-1} \left( \frac{\sqrt{b}}{s_1} \right) ; \quad \gamma_2 = \cos^{-1} \left( \frac{\sqrt{g}}{s_1} \right) \\ \beta_3 = \cos^{-1} \left( \frac{\sqrt{b}}{s_1} \right) ; \quad \gamma_3 = -\cos^{-1} \left( \frac{\sqrt{g}}{s_1} \right) \\ \beta_4 = -\cos^{-1} \left( \frac{\sqrt{b}}{s_1} \right) ; \quad \gamma_4 = -\cos^{-1} \left( \frac{\sqrt{g}}{s_1} \right) \end{array} \right. \quad (23)$$

In most of the case, this ambiguity as to whether the angle is positive or negative can be solved simply by hypothesizing that the movement of the periodic pattern remains continuous. However, by switching from a scaled orthographic projection to a perspective one, an unambiguous set of solutions for the 6-DOF pose can be found.

#### IV. EXTENSION TO 6-DOF POSE MEASUREMENT UNDER PERSPECTIVE PROJECTION WITH LONG FOCAL LENGTHS

As noted in the previous section, orthographic projection conserves the ratio of the imaged scene without regard for the distance from the camera of the points of the scene (as presented in the Fig. 4). Switching to a perspective projection causes the points of the scene to be projected according to the focal distance (pinhole model). This effect can be seen in Fig. 5, where the periods of an inclined periodic pattern yield different imaged periods  $p_1$  and  $p_2$  (in pixels). This projection also allows the measurement of the average distance of the observed periodic pattern from the camera (given its focal distance).

As illustrated in Fig. 5, retrieving the evolution of the pixelic period size inside the image, where larger pixelic periods denote the periodic pattern's closer proximity to the camera, allows a measurement of the absolute pose orientation of the pattern. Indeed, contrary to the case of an orthographic projection, the phase along each direction no longer increases linearly, as shown on Fig. 6. Since the period of the pattern is given by the first derivative of the phase (written  $\Psi_i$ ), by studying the derivative of the period (written  $\Upsilon_i$ ), an absolute angle measure can be performed. A more comprehensive way to visualize the evolution of the different derivatives of the phase can be seen in the first supplementary material video, where the evolution

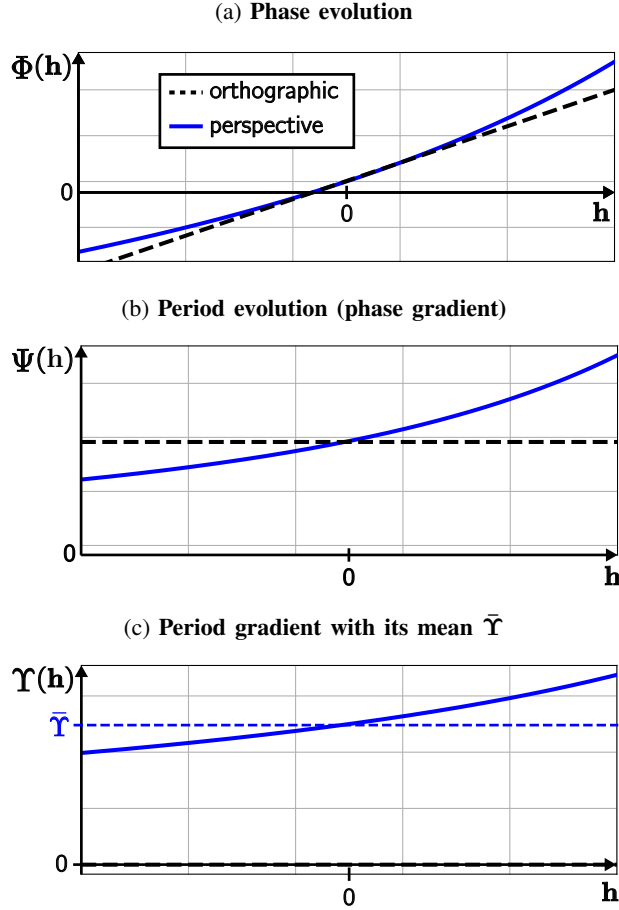


Fig. 6: Line projection of a tilted pattern through perspective projection with its phase evolution and its derivatives. (a) phase evolution along direction  $\mathbf{h}$  in the image and highlights the impact of the perspective projection on the phase evolution compared to an orthographic projection. (b) first derivative of the phase along  $\mathbf{h}$  and by extension the observed period evolution of the periodic pattern. (c) second derivative of the phase that allows to find the angle sign with the sign of its mean

of the pattern orientation  $\beta$  is imaged through a perspective projection with a short focal. Summarizing the different phase image gradients that are considered gives:

$$\begin{cases} \Psi_i = \frac{d\Phi_i}{dh_i} \\ \Upsilon_1 = \frac{d\Psi_1}{du} = \frac{d^2\Phi_1}{du^2} \end{cases} \quad (24)$$

As presented in Fig. 6.(b), in the case of an orthographic projection, the first derivative is a constant that represents the imaged pixelic period of the pattern. However, in the perspective case, this evolution is non linear and depends on the angle of the pattern. If this evolution along each main direction ( $\mathbf{h}_1, \mathbf{h}_2$ ) is increasing, the pattern is tilted towards the camera (respectively, if the period is decreasing then the pattern is tilted away from the camera). Thus, the study of the sign of this period evolution (i.e. its gradient) gives an absolute angle retrieval.

$$\begin{cases} \Upsilon_1 > 0 \Leftrightarrow \beta > 0 \\ \Upsilon_2 > 0 \Leftrightarrow \gamma > 0 \end{cases} \quad (25)$$

In order to measure the derivatives of the phase evolution along each direction (giving the period evolution along each main direction of the pattern), an implicit change of referential from the camera frame to the pattern is done.

By considering the two phase maps, their gradients in the pattern axis base ( $\mathbf{h}_1, \mathbf{h}_2$ ) is given by:

$$\Psi_i = \frac{d\Phi_i}{dh_i} = \frac{\partial\Phi_i}{\partial x_c} \cdot \frac{\partial x_c}{\partial h_i} + \frac{\partial\Phi_i}{\partial y_c} \cdot \frac{\partial y_c}{\partial h_i} \quad (26)$$

$\frac{\partial \Phi_i}{\partial x_c}$  and  $\frac{\partial \Phi_i}{\partial y_c}$  can be calculated with a classic image gradient method consisting of a convolution product between a kernel and the phase map images. Presented method relies on the Sobel operator that gives the following derivatives:

$$\frac{\partial \Phi_i}{\partial x_c} = \begin{bmatrix} 1 & 2 & 1 \\ 0 & 0 & 0 \\ -1 & -2 & -1 \end{bmatrix} \otimes \Phi_i \quad (27)$$

and

$$\frac{\partial \Phi_i}{\partial y_c} = \begin{bmatrix} 1 & 0 & -1 \\ 2 & 0 & -2 \\ 1 & 0 & -1 \end{bmatrix} \otimes \Phi_i \quad (28)$$

where  $\otimes$  is the bi-dimensional convolution product. Since this first  $\Psi_i$  gradient calculation was made to shift from the camera frame referential to the pattern's one, the next gradient calculation ( $\Upsilon_i$ ) is more straightforward and can be expressed directly as the gradient of the obtained image along each direction.

Finally, to retrieve the sign of the pattern orientation, the sign of  $\tilde{\Upsilon}_i$  along each direction can be studied as:

$$\begin{cases} \text{sign}(\beta) = \text{sign}(\tilde{\Upsilon}_1) = \text{sign} \left( \frac{1}{w \cdot h} \sum_{i=0}^{w-1} \sum_{j=0}^{h-1} \Upsilon_1 \right) \\ \text{sign}(\gamma) = \text{sign}(\tilde{\Upsilon}_2) = \text{sign} \left( \frac{1}{w \cdot h} \sum_{i=0}^{w-1} \sum_{j=0}^{h-1} \Upsilon_2 \right) \end{cases} \quad (29)$$

With this, a direct choice among the set of solutions for  $\beta$  and  $\gamma$  orientations can be made to provide an absolute angle retrieval.

Finally, to ensure a complete pose measurement, the distance of the pattern to the camera  $z$  can be calculated with the perspective projection, given the equivalent focal distance  $f$  of the camera and the scale factor  $s$ :

$$z = \frac{f}{s} \quad (30)$$

As explained at the beginning of this section, this method of unambiguous pose measurement relies on the non-linearity of the two phase maps. On the other hand, presented method uses the assumption of a linear phase, used to compute the two phase planes equations. Therefore depending on the application, a trade-off between a purely orthographic projection resulting in a highly resolute but ambiguous pose measure and a highly perspective projection resulting in a less resolute pose measurement but unambiguous needs to be found.

With the already discussed method of absolute in-plane pose retrieval shown in section II and the equations for absolute pose measurement presented in the two previous sections, a full pose can be deduced directly from the Fourier analysis of the pattern.

The next sections will study the capabilities and limitations of the presented method of pose measurement in order to validate it both with numerical simulation and by experimentation.

## V. NUMERICAL PERFORMANCES EVALUATION

The presented method has been programmed in C++ for computation efficiency and can carry the full pose measurement of encoded periodic patterns with a frequency up to 25 Hz (for images sizing  $512 \times 512$  px) with a standard computer (i7 processor at 3.7 GHz with 32 Go of RAM). For larger images ( $1024 \times 1024$  px), a frequency of 5 Hz is achieved. Along with the pose measurement implementation, this library can also generate images of periodic patterns along the 6-DOF that can be used for simulation purposes. More insights on the computation time can be found on the library's reference website<sup>1</sup>. With this tool, a closed loop between generated patterns and their pose measure can be done to evaluate numerical accuracy.

### A. Orthographic range evaluation

The first evaluation of the method aims to identify the available range of measure for the two off-axis angles in the orthographic case by simulating periodic pattern poses with  $\beta$  and  $\gamma$  rotations. Both angles are set to evolve in the  $[0, \frac{\pi}{2}]$  rad. range and by studying the error between the sent pose and the computed one, a refined angle measurement range with an error lower than  $1 \mu\text{rad}$ . can be found.

To perform this simulation, perfectly simulated patterns images with a 25 px period are generated at the following poses:  $[0, 0, 0, 0, \beta, \gamma]$  with  $\beta$  and  $\gamma$  set to evolve in the  $[0, \frac{\pi}{2}]$  rad. range. As previously explained in section III-D, under orthographic projection, off-axis angle measurement is the same for positive and negative values of rotation. Thus, simulations can only

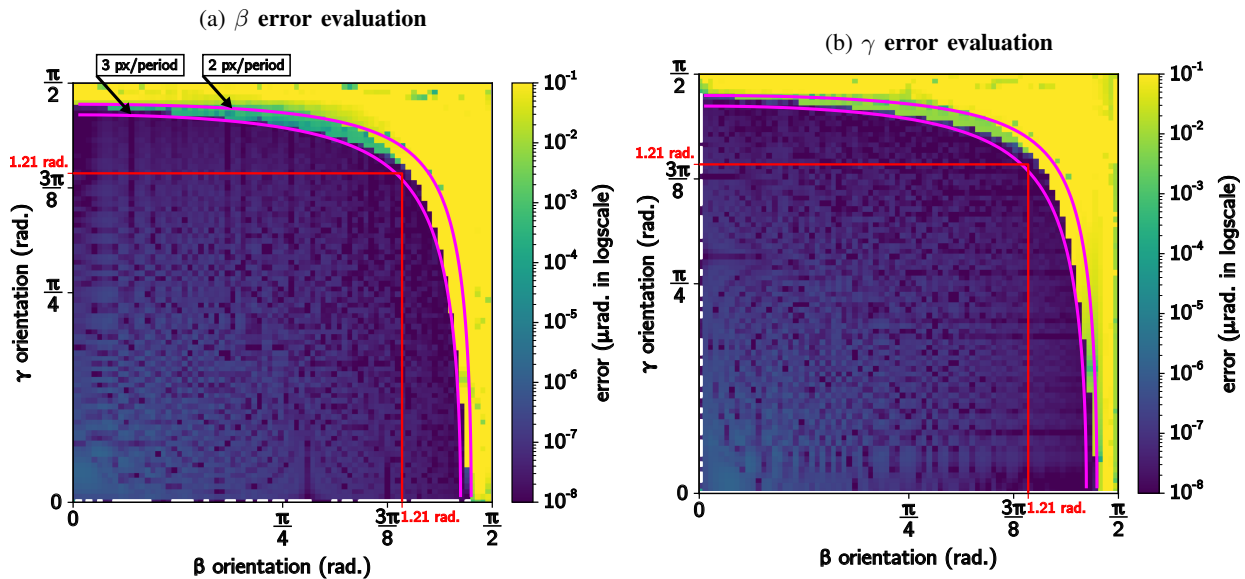


Fig. 7: Off-axis angles error maps when the pattern (period 25 px) is tilted along  $\beta$  and  $\gamma$  orientations in the  $[0, \pi/2]$  range. (a) presents the error of evaluation of the  $\beta$  angle and (b) presents the  $\gamma$  error map. The area where both angles are measured with an error lower than 1  $\mu$ rad. is denoted in red in both sub-figures. The black lines show the angles for which the apparent period is respectively 3 and 2 pixels long.

focus on the case where  $\beta$  and  $\gamma$  evolve on the positive side. This simulation can be treated as a map with the  $\beta$  angle evolving along the  $x$  axis and the  $\gamma$  angle along the  $y$  axis, as shown in Fig. 7.

Fig. 7 summarizes the relative error evolution of each angle measurement as the two maps' results. These error maps provide information about the relative error between the sent pose and the computed one. When both  $\beta$  and  $\gamma$  angles are in the  $[0, 1.21]$  rad. range (in the red square), the level of error presents a standard deviation of  $1.81 \cdot 10^{-7}$  rad. for both measures.

The first black line represents the limit of the peaks detection of the algorithm when the second one stands for the Shannon limit. Indeed, when the pattern is rotated the apparent period on the image is equal to  $s\lambda \cos(\beta) \cos(\gamma)$ . If this value is below 2 px, the frequency of the pattern is not detectable (Nyquist-Shannon sampling theorem). The peak localization in the Fourier transform is no longer efficient when this value is below 3 px that is very close to the theoretical limit.

This measurement range can be much appreciated in the second supplementary video where pseudo-periodic pattern images are generated at various off-axis angles in the  $[0, \frac{\pi}{8}]$  rad. range. This short video also shows that the level of error between sent angle and computed one doesn't exceed 1  $\mu$ rad. most of the time even when considering an encoded periodic pattern. The supplementary video 3 presents an other view of the available measurement range. This one presents an encoded periodic pattern rotating along the  $\beta$  angle from 0 to  $\frac{\pi}{2}$  rad. This video demonstrates the underlying base of the pose measurement method, that lean on the detection of the two main spectrum peaks. As it can be seen in this one, as long as the visible period of the pattern is below the Shannon limit, the pose is measured with a great accuracy. These two videos also provide a more comprehensive way of understanding how the Fourier spectrum and the main peaks used in the pose measurement process move when large off-axis angles are considered.

### B. Random 3D pose simulation under orthographic projection

To validate the method's performance along the 6 studied degrees of freedom, a set of 1000 random images has been generated. The considered range is the in-plane  $(x, y, \alpha)$  one provided by the encoded target and the range studied in the previous section for off-axis angles  $(\beta, \gamma)$ . To evaluate the last considered degree of freedom  $s$  (the scale factor), the apparent period is randomly set between 8 and 12 px. In short, the patterns is generated according to following parameters:

- $(x, y) \in [0, 10^4]$  px.
- $\alpha \in [0, 2\pi)$  rad.
- $(\beta, \gamma) \in [0, \frac{3\pi}{8}]$  rad.
- $\lambda \cdot s \in [8, 12]$ .

The results of this simulation can be visualized as six separate histograms revealing the error of the pose measurement; these are presented in Fig. 8. These results show that the off-axis angles do not impact the in-plane measure with a resolution of less than  $1/1000^{th}$  of a pixel in translation and  $0.2 \cdot 10^{-6}$  rad. in orientation. The two considered off-axis angles  $\beta$  and  $\gamma$  reveal a

<sup>1</sup><https://projects.femto-st.fr/vernier/en>

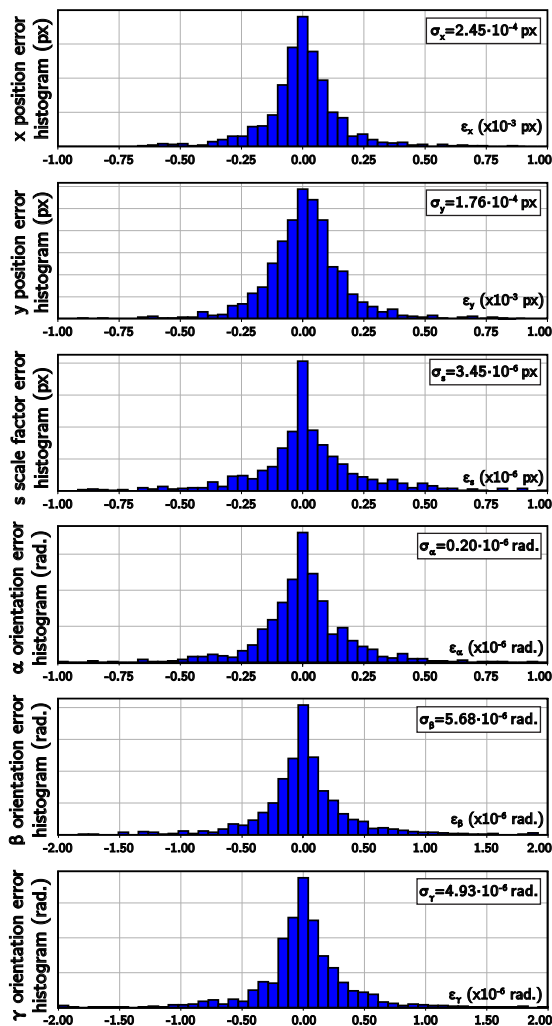


Fig. 8: Error measure between sent pose and computed one with a data set of 1000 randomly generated poses

resolution around  $5 \cdot 10^{-6}$  rad. and an error in the scale factor measure of around  $6.94 \cdot 10^{-4}$ . Along with the histogram plot of errors, the dataset used for this study can be found in Supp. Mat. 2.

### C. Comparison with PnP pose estimation

A last simulation aiming to compare the performance of proposed method with a classic Perspective-n-Point (PnP) pose estimation is put in practice. In order to make a fair comparison, the same set of images of a circle grid has been used for both methods. The pose of the circular grid is estimated via the PnP pose estimation algorithm implemented in OpenCV (with the two commands `findCirclesGrid` and `solvePnP2`). Along with the comparison of the presented method with a classical pose estimation method, this simulation aims also to study the impact of the perspective projection on the resolution of the measure. Indeed, as discussed in the last part of section IV, the non-linearity of the phase maps induced by shorter focal lengths may result in less resolute measures. For both methods, the simulations also explore the impact of the pattern period on the achieved resolution on the interval  $s\lambda \in [6, 70]$  px.

The parameters to generate the set of grid images can be organized in three parts that are listed below:

- 4 different off-axis angles (0.01, 0.1,  $\pi/8$  and 1 rad.)
- 4 different focal lengths (orthographic, 300, 50 and 16 mm)
- The pixelic period set to increase in the  $[6, 70]$  px range

The resulting generated set of images from these parameters are available for download<sup>3</sup>

Fig. 9 presents the results of this comparison with a lin-log scale. Concerning the proposed method, Fig. 9.(a) confirms that its resolution varies with the number of periods visible in the image. Indeed, no matter the focal length or the off-axis angle

<sup>2</sup>OpenCV PnP solver documentation available here: [https://docs.opencv.org/3.4/d9/d0c/group\\_\\_calib3d.html](https://docs.opencv.org/3.4/d9/d0c/group__calib3d.html)

<sup>3</sup><https://sourcesup.renater.fr/www/vernierlibrary/data/>

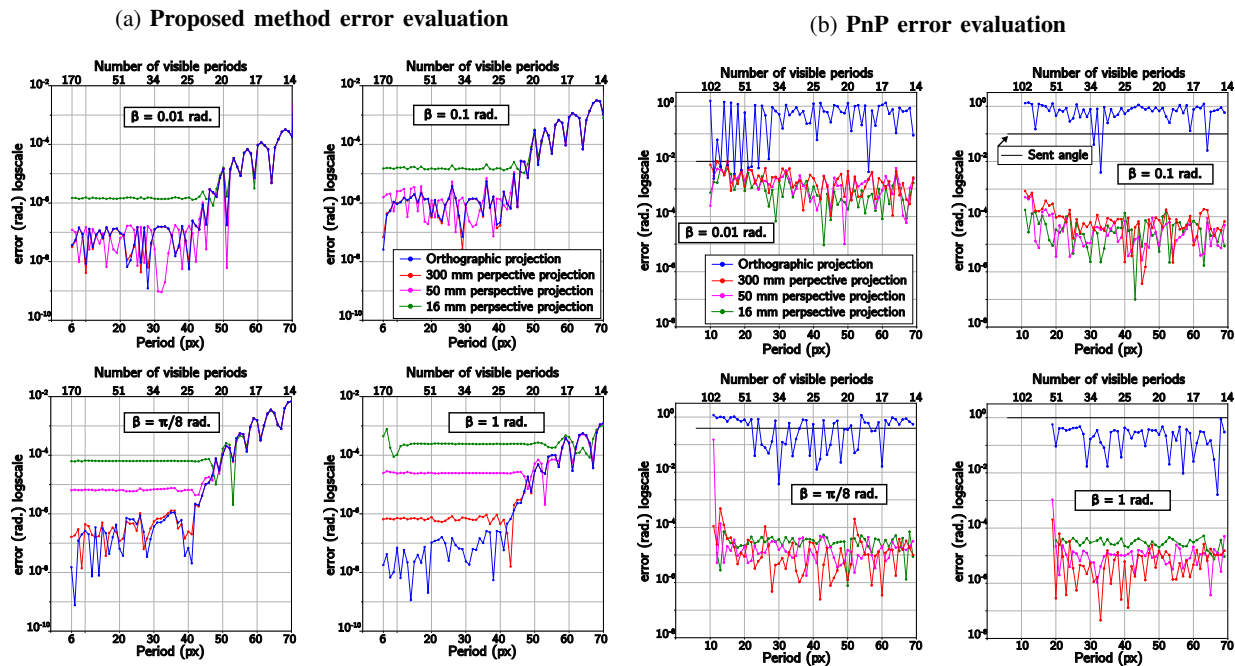


Fig. 9: Off-axis angle measurement error in function of the pixelic period of the periodic pattern for a set of four focal lengths and of four off-axis angles. (a) proposed method; (b) OpenCV PnP method.

used, below 25 visible periods (or over a visible pixelic period of 40 px), a significant decrease in the resolution is observed. When the number of visible periods is over 25, a resolution below  $10^{-6}$  rad. can be achieved. This resolution also depends on the focal length used and, as depicted in the sub-figures, the resolution decreases as the focal length also decreases and this impact of the focal length is stronger for larger out-of-plane angles. In comparison, as shown in Fig. 9.(b), the classic PnP method isn't impacted by the focal length used nor by the increase of the off-axis angles. Indeed shown resolution remains below  $10^{-4}$  rad. However, since this method uses a perspective projection to estimate the pose, it is normal to see a very low resolution when an orthographic projection is involved. This comparison between the two methods highlights the better sensitivity of the proposed phase-based method, especially for small out-of-plane angles. As one can see, for an off-axis angle of 0.01 rad. a resolution of  $10^{-7}$  rad. is achieved to be compared to the  $10^{-3}$  rad. achieved by the PnP method. The fact that the proposed method considers the phase of every image pixel rather than only the centers of geometrical features explains partly such a discrepancy.

## VI. EXPERIMENTAL VALIDATION

To validate both the high-resolution pose measure and the available range of measure along the two off-axis angles  $\beta$  and  $\gamma$ , and along the optical axis  $z$ , two main experiments were designed.

### A. Validation under orthographic projection

To demonstrate the proposed method's experimental performance, multiple setups have been put in practice. The first experimental setup uses a camera (IDS UI-3280CP) and a 5x microscope objective (Optem with a numerical aperture of 0.14 and a depth of field of 29  $\mu\text{m}$ ) coupled with a 1.5x microscope tube (Optem) to record images of a pseudo-periodic encoded pattern printed on a glass plate with a period of 9  $\mu\text{m}$ . The plate was placed on a single axis rotary stage (Smaract SR2013 with a closed loop resolution of 0.5  $\mu\text{rad}$ ). The camera is set to record images at a constant frame-rate of 20 images per second, encoded at a depth of 12 bits. The binary encoded pattern and the rotary stage are placed on a  $xyz$  manual axis stage in order to situate the observed target perpendicular to the optical axis of the microscope objective. Fig. 10 and supplementary material 4 summarizes the disposition of the main elements of this experimental setup.

1) *Resolution evaluation*: A first step in finding the real resolution of the off-axis angular determination is to study the static noise measure. This one is measured with the setup detailed above, with the rotary stage switched off during a 40-second run, resulting in an 800-image analysis. The measure of the noise is collected by computing the standard deviation (std) of each of the computed angles. The results, which are presented in Tab. I indicate a static noise of around one tenth of a milliradian and demonstrate the maximal resolution attainable with this setup.

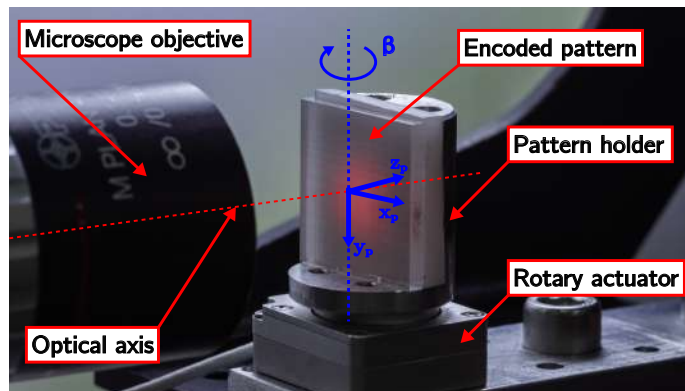


Fig. 10: Experimental setup put in practice to validate the resolution performances of the off-axis angle measurement

TABLE I: Standard deviation levels observed on each measured degree of freedom during a static test of 40 seconds (800 images)

DOF	std	unit
$x$	8.07	nm
$y$	16.02	nm
$s$	$0.42 \cdot 10^{-6}$	px/mm
$\alpha$	3.25	$\mu\text{rad.}$
$\beta$	0.1205	mrad.
$\gamma$	0.1181	mrad.

To estimate the angular resolution achievable via the presented method, a square signal consisting of steps of 0.2 mrad. is sent to the rotary stage at a constant rate of 0.25 Hz, thus allowing an acquisition of 40 images per step. Computed angles are presented in Fig. 11.(a). and confirm the resolution capabilities of angle determinations that lie below 0.1 mrad. This figure also presents the computed mean angle and the error bar for each step of the sent square signal. Differences between the resolution evaluated with generated images in the previous section and the resolution presented in Table. I are largely attributable to environmental disturbances such as vibrational noise coming from the experimental setup and from experiment room. A differential analysis of the set of images with the same setup demonstrated that, in the in-plane measurement case, environmental disturbances are responsible for more than 93% of the total variance of errors Andre et al. (2020).

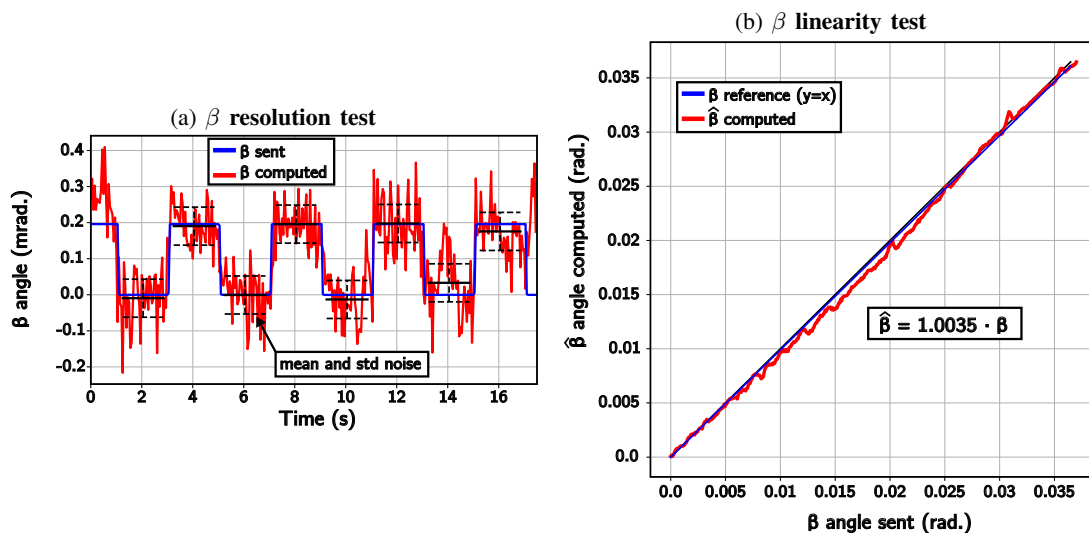


Fig. 11: (a)  $\beta$  resolution evaluation, steps of 2 seconds (containing 40 images per step ) run over 40 seconds. (b) Linearity evaluation experiment along  $\beta$  orientation

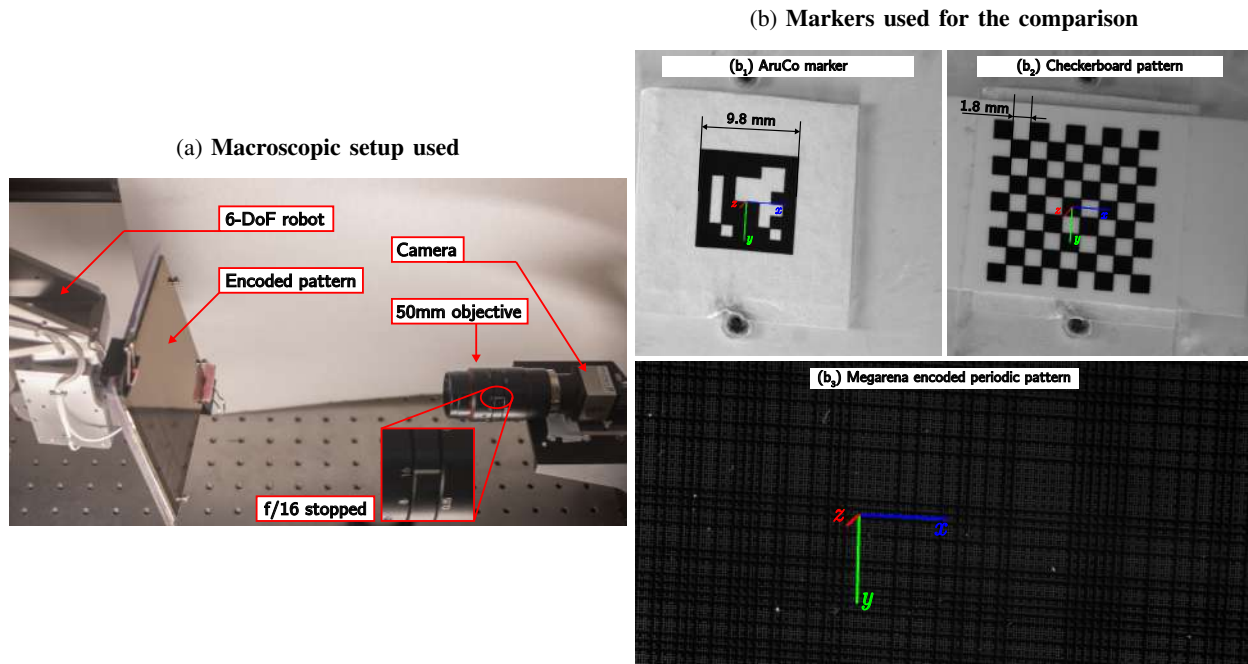


Fig. 12: (a) Experimental setup used for the large range pose measurement under perspective projection. (b<sub>1</sub>) and (b<sub>2</sub>) show the two markers used for the pose measurement comparison with the pseudo-periodic pattern (b<sub>3</sub>) used with the presented method

2) *Linearity and range of measure evaluation*: To complete the evaluation of the method's performance, a test of linearity is conducted. Since this article's primary contribution is to present a novel means of retrieving a 6-DOF pose at the micro-scale, the range of measure presented in the simulation section of  $3\pi/8$  can't be achieved with experiments involving a microscope. Indeed this range of measure is inherently shortened by the depth of field of used microscope objectives. The one used for the experiment has a depth of field of  $28 \mu\text{m}$ , with this, any angle higher than  $0.03 \text{ rad}$ . will result in a blurred image on each side of the pattern. The problem raised by this blur appearing at the borders of acquired images is a weaker spectrum peak energy that leads to a less resolute measure. The experimental validation of the linearity will therefore be made by sweeping the target in the range of  $[0; 0.03] \text{ rad}$ .

The results, presented in Fig. 11.(b), highlights the high linearity of the orientation measurement, with an error factor of approximately  $0.35\%$  in the evaluated range with regards to the inherent limitations of the experimental setup and its environment,

### B. Validation under perspective projection with long focal length

In order to validate the 6-DOF pose measurement method presented in section IV, another experiment involving a macroscopic setup is put in practice.

This setup, presented in Fig. 12, comprises a 6-DOF serial robot (with 3 prismatic and 3 rotational Smaract actuators), a macro objective (Kowa 50 mm) and the same camera that was used in the experiments previously described. As this set of experiments is meant to validate the pose measure at a larger scale, an encoded periodic pattern with a  $140 \mu\text{m}$  period is placed on the end effector of the robot (the resulting acquired images of the pattern can be seen in Fig. 12.(b<sub>3</sub>)). To maximize the depth of field (and therefore the available range of measure) along the optical axis  $z$ , the objective is stopped at  $f/16$ . The capabilities of the lens include an available range of focusing around  $10 \text{ mm}$ ; the closing of the aperture results in sharper acquired images, in addition to the increased depth of field. The objective and the camera are placed at a distance of  $30 \text{ cm}$  from the robot, allowing a perspective projection weak enough to carry the localization of the peaks in the Fourier transform with sufficient accuracy. However, the robot's accuracy is unknown and experiments are carried out to broaden the measure by considering larger rotations and displacements under perspective projection.

1) *Evaluation along the  $z$  axis*: The first experiment involving this setup is to insure the validity of the pose measurement along the optical axis  $z$ . To do this, a trajectory composed by a translation along the  $x$  and  $y$  axis (resulting in the logo pattern presented in Fig. 13.(c)) and by a sinusoidal translation along the  $z$  axis (as shown in Fig. 13.(b)) is sent to the robot. The chosen objective and aperture allow a range of  $\pm 5 \text{ mm}$  around the focal plane in which the pattern would stay sharply in focus, and therefore, the sinusoidal trajectory sent along the  $z$  axis is set to evolve in the  $[-5; 5] \text{ mm}$  range.

The resulting curves show that the measure is qualitatively smooth all along its path in the  $z$  direction and is unaffected by the  $x, y$  position of the pattern. Unfortunately, since the measure of the robot is of a lower resolution than the tested pose

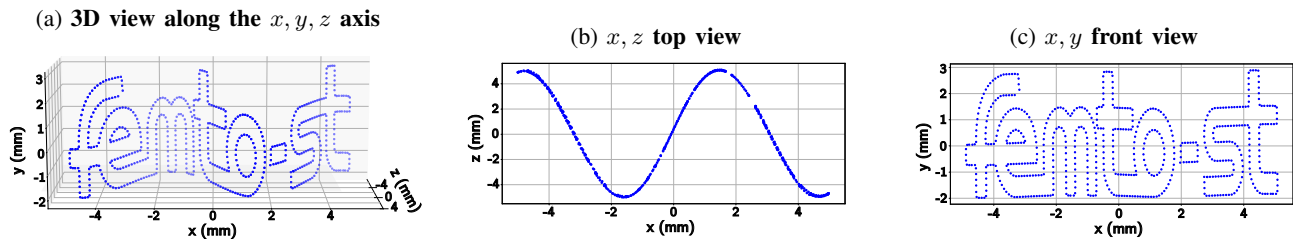


Fig. 13:  $x, y, z$  trajectory sent to the robot presenting both a 3D global view (a), a top view (b) highlighting the  $z$  evolution of the pattern and a front view (c) showing the  $x, y$  evolution of the pattern

measure, no pertinent quantitative comparison can be done with this setup. However, with the considered displacement range of 10 mm and the measured position shown in Fig. 13.(b), a resolution of at least 0.1 mm can be deduced. In pixelic terms, this sub-millimetric resolution corresponds  $0.5 \cdot 10^{-3}$  pixels resolution, which confirms the method's global performance in depth estimation. As explained in the presentation of the experimental setup, the considered objective provides a measurement range of  $\pm 5$  mm around the focal plane when closed at  $f/16$ , but this range could easily be extended by using an objective with a larger depth of focus.

2) *6-DOF trajectory pose measurement*: The final experiment is set up to validate the pose measure under perspective projection along the 6 degrees of freedom simultaneously. For this purpose, this setup also make use of the 6-DOF serial robot described above. To generate a trajectory that would evolve in the whole studied range, each degree of freedom is assigned to a sinusoidal input with slightly different frequencies and phase shifts resulting in the global 6-DOF trajectory presented in Fig. 14. Using this trajectory generation method ensures that the majority of the range is studied during the experiment and that computed results are homogeneous within the entire range.

As presented in the introduction of this paper, there are other viable methods of single-camera pose measurement using the coplanar constraint of fiducial markers, such as chessboards and ArUco markers. This experiment is therefore also designed to compare these alternatives' capabilities with those of the presented method. To that end, a chessboard with squares sizing 1.8 mm and an ArUco marker sizing 9.8 mm are printed and placed on the end effector of the robot. The results of the acquired images, as well as the sizes of the different markers can be seen in Fig. 12.( $b_1$ ), ( $b_2$ ).

To keep the ArUco fiducial marker and the chessboard in the camera frame, translations along the  $x$  and  $y$  axis are set in the  $[-5; 5]$  mm range. The range of displacement along the  $z$  axis is also set to stay within  $[-5; 5]$  mm around the focal plane (the same range used in the prior experiment). As this experiment's goals include the validation of the method in cases where larger off-axis angles are implied, sent angles are set in the  $[-10, 10]$  degree range ( $[-0.17, 0.17]$  rad.).

The results of the pose measurement are presented in Fig. 14, along with different views that help elucidate the global 6-DOF trajectory evolution of the robot. The validation of the method therefore stems from the global evolution of the trajectory, which remains unchanged across the three tested methods. However, while ArUco markers and chessboards tend to work better with wider perspective projection and lower distances, as discussed in section V-C, and as shown by Abawi et al. (2004), and Pentenrieder et al. (2006), their measured poses present much more noise than the presented method, especially for off-axis orientations  $\beta$  and  $\gamma$  and for  $z$  depth measure. In fact, relying on the highly redundant periodic information of the pattern processed in the Fourier domain reduces the noise of the resulting computed poses and, as shown on Fig. 14, greatly increases their resolution.

## VII. CONCLUSION AND PROSPECTS

This article proposed a novel method of measuring the pose of periodic patterns by analyzing the Fourier spectrum of the acquired images. The presented method can be applied in orthographic projection with a 5-DOF pose measures with ambiguities to determine the off-axis angles and the scale factor. This can be solved by using a perspective projection with long focal lengths that leads to a full and unambiguous pose measure, including a measure of depth.

By validating the method through simulations, this research demonstrated a range of measure of  $\pm 3\pi/8$  rad. (1.21 rad.). These simulations also permitted the demonstration of high-resolution capabilities of the measure with an error level of less than  $1/1000^{th}$  of a pixel in translation, 0.2  $\mu$ rad for in-plane orientation, and 1  $\mu$ rad for off-axis orientations.

Presented method was numerically compared to the widely used PnP method for a set of four focal lengths, four out-of-plane angles and on a pixelic period interval of  $[40, 70]$  px. The proposed spectral method outperforms the OpenCV PnP implementation, especially in the orthographic projection case and at low out-of-plane angles. The fact that the proposed

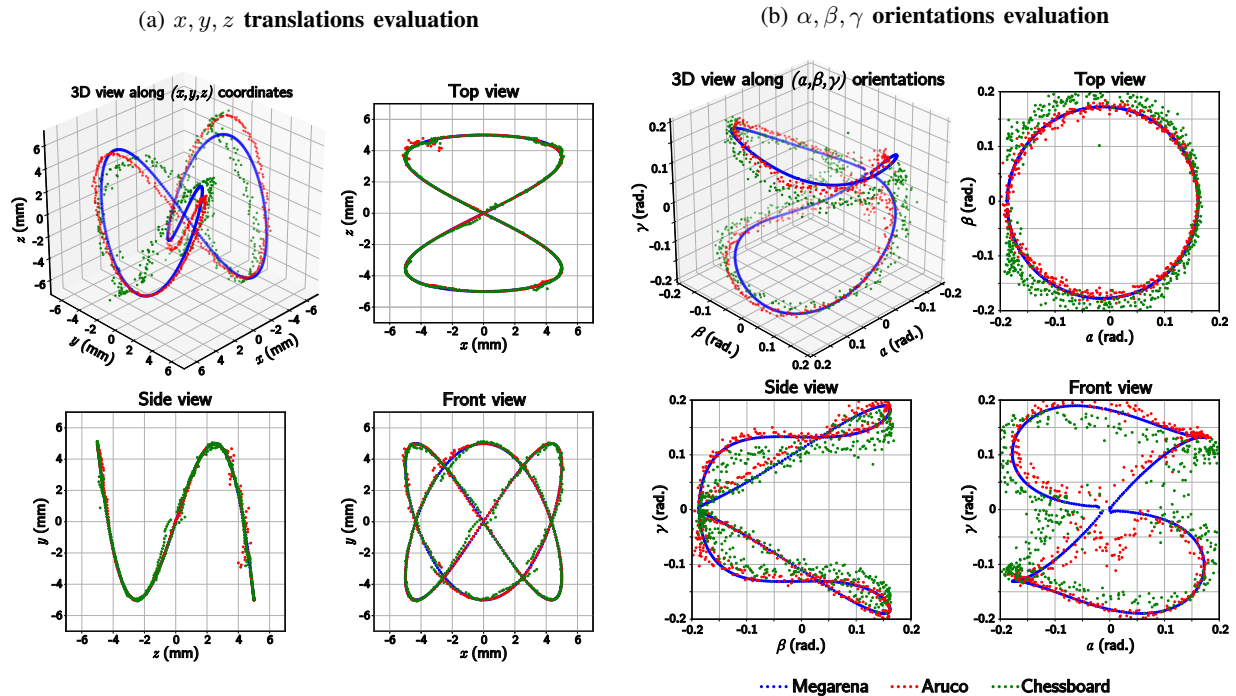


Fig. 14: 6-DOF trajectory evaluation with different sinusoidal inputs made with a pseudo-periodic pattern, a chessboard and an ArUco marker distributed in two sub-figures for (a) the translations and (b) the orientations measures

method considers the phase of every image pixels rather than only the centers of geometrical features explains partly such a discrepancy.

The method was investigated experimentally within the range allowed by the lenses used and revealed a resolution of 0.1 mrad. and a linearity of 0.035% for the off-axis orientation measure. Finally, the proposed method was applied to a perspective projection experiment, revealing a resolution of the pattern pose measure along the  $z$  axis lower than 0.1 mm. To conclude, the method was tested through a comparison experiment implying other well known fiducial markers and proved the measure to be more resolute than other methods.

As shown in the different experiments, the encoded pattern can be scaled and applied to various camera projection models, leading to either a 5-DOF or a 6-DOF pose measure, and can therefore be addressed to different fields of application. In microrobotics, for instance, the pattern might be used to control the precise localization of microrobots, viewed under microscopes for micro assembly issues. On a larger scale, the method could also be applied to control the pose of robots along the 6-DOF and offer an interesting alternative with better resolution to pre-existing markers. With the large covering of the pattern in the image and with the knowledge of its physical period, it is possible to carry high resolution calibration both for robots and for camera used. Finally, this method offers a good compromise between interferometry and visual pose estimation by requiring fewer material than interferometers while presenting better resolutions than fiducial-marker-based methods.

A major prospect for the presented work is its enlargement under a wider perspective by considering different forms of Fourier analysis that could function with non-linear projection of periodic pattern evolution. This non-linear analysis in the Fourier domain could also lead to new applications which would be less focused on the micro-scale such as camera calibration following the work of Chen et al. (2020), who used the phase planes to robustly detect the points of a grid before solving the PnP problem.

#### ACKNOWLEDGMENT

This work was supported by Région Bourgogne Franche-Comté, by the ANR project Holo-Control (ANR-21-CE42-0009), by the I-SITE BFC project HoloNet (ANR-15-IDEX-03), by Cross-disciplinary Research (EIPHI) Graduate School (ANR-17-EURE-0002). The encoded target was realized thanks to the RENATECH technological network and its FEMTO-ST facility MIMENTO. The experiments was conducted within the ROBOTEX robotics network (ANR-10-EQPX-44-01) and its FEMTO-ST micro-nano-robotics center. Authors acknowledge G. Jutzi, L. Robert, M. Suarez and L. Gauthier-Manuel for technological and experimental assistance.

## CONFLICT OF INTEREST

The authors declare that they have no conflict of interest.

## REFERENCES

- Abawi DF, Bienwald J, Dorner R (2004) Accuracy in optical tracking with fiducial markers: an accuracy function for artoolkit. In: Third IEEE and ACM International symposium on mixed and augmented reality, IEEE, pp 260–261
- André AN, Sandoz P, Jacquot M, Laurent GJ (2020) Robust, precise and scalable: A phase-encoded pattern for visual  $x, y, \theta$  positioning. In: 2020 International Conference on Manipulation, Automation and Robotics at Small Scales (MARSS), IEEE, pp 1–5
- André AN, Sandoz P, Mauze B, Jacquot M, Laurent GJ (2020) Sensing one nanometer over ten centimeters: A micro-encoded target for visual in-plane position measurement. *IEEE/ASME Trans Mechatronics* 25(3):1193–1201, DOI 10.1109/TMECH.2020.2965211
- André AN, Sandoz P, Mauzé B, Jacquot M, Laurent GJ (2021) Robust phase-based decoding for absolute  $(x, y, \theta)$  positioning by vision. *IEEE Transactions on Instrumentation and Measurement* 70:1–10, DOI 10.1109/TIM.2020.3009353
- Azar ER, Feng C, Kamat VR (2015) Feasibility of in-plane articulation monitoring of excavator arm using planar marker tracking. *Journal of Information Technology in Construction (ITcon)* 20(15):213–229
- Bay H, Tuytelaars T, Van Gool L (2006) Surf: Speeded up robust features. In: European conference on computer vision, Springer, pp 404–417
- Bomaré G, Hochhalter J, Ruggles T, Cannon A (2017) Increasing accuracy and precision of digital image correlation through pattern optimization. *Optics and Lasers in Engineering* 91:73–85
- Bouguet JY (2004) Camera calibration toolbox for matlab. [http://www.vision.caltech.edu/bouguetj/calib\\_doc/index.html](http://www.vision.caltech.edu/bouguetj/calib_doc/index.html)
- Bruckstein AM, Holt RJ, Huang TS, Netravali AN (1999) Optimum fiducials under weak perspective projection. *International Journal of Computer Vision* 35(3):223–244
- Bruckstein AM, Holt RJ, Huang TS, Netravali AN (2000) New devices for 3d pose estimation: Mantis eyes, agam paintings, sundials, and other space fiducials. *International Journal of Computer Vision* 39(2):131–139
- Chen X, Fan R, Wu J, Song X, Liu Q, Wang Y, Wang Y, Tao B (2020) Fourier-transform-based two-stage camera calibration method with simple periodical pattern. *Optics and Lasers in Engineering* 133:106121
- Chen ZH, Huang PS (2016) A vision-based method for planar position measurement. *Measurement Science and Technology* 27(12):125018
- Chu HK, Mills JK, Cleghorn WL (2012) Dual-arm micromanipulation and handling of objects through visual images. In: 2012 IEEE International Conference on Mechatronics and Automation, IEEE, pp 813–818
- Collins T, Bartoli A (2014) Infinitesimal plane-based pose estimation. *International journal of computer vision* 109(3):252–286
- Didier JY, Ababsa FE, Mallem M (2008) Hybrid camera pose estimation combining square fiducials localization technique and orthogonal iteration algorithm. *International Journal of Image and Graphics* 8(01):169–188
- Drummond T, Cipolla R (2002) Real-time visual tracking of complex structures. *IEEE Transactions on pattern analysis and machine intelligence* 24(7):932–946
- Fiala M (2005) Artag, a fiducial marker system using digital techniques. In: 2005 IEEE Computer Society Conference on Computer Vision and Pattern Recognition (CVPR'05), IEEE, vol 2, pp 590–596
- Garrido-Jurado S, Muñoz-Salinas R, Madrid-Cuevas FJ, Marín-Jiménez MJ (2014) Automatic generation and detection of highly reliable fiducial markers under occlusion. *Pattern Recognition* 47(6):2280–2292
- Guelpa V, Laurent GJ, Sandoz P, Zea JG, Clévy C (2014) Subpixelic measurement of large 1d displacements: Principle, processing algorithms, performances and software. *Sensors* 14(3):5056–5073
- Kato H, Billingham M (1999) Marker tracking and hmd calibration for a video-based augmented reality conferencing system. In: Proceedings 2nd IEEE and ACM International Workshop on Augmented Reality (IWAR'99), IEEE, pp 85–94
- Kim JA, Kim JW, Kang CS, Jin J (2018) Note: An absolute  $xy-\theta$  position sensor using a two-dimensional phase-encoded binary scale. *Review of Scientific Instruments* 89(4):046105
- Kim YS, Yang SH, Yang KW, Dagalakis NG (2015) Design of mems vision tracking system based on a micro fiducial marker. *Sensors and Actuators A: Physical* 234:48–56
- Li H, Zhu B, Chen Z, Zhang X (2019) Realtime in-plane displacements tracking of the precision positioning stage based on computer micro-vision. *Mechanical Systems and Signal Processing* 124:111–123
- Liu A, Marschner S, Snavely N (2016) Caliber: Camera localization and calibration using rigidity constraints. *International Journal of Computer Vision* 118(1):1–21
- Liu J, Gong Z, Tang K, Lu Z, Sun Y (2013) Locating end-effector tips in automated micromanipulation. In: 2013 IEEE International Conference on Robotics and Automation, IEEE, pp 1724–1729
- Loing V, Marlet R, Aubry M (2018) Virtual training for a real application: Accurate object-robot relative localization without calibration. *International Journal of Computer Vision* 126(9):1045–1060

- Marturi N, Tamadazte B, Dembélé S, Piat N (2016) Image-guided nanopositioning scheme for sem. *IEEE Transactions on Automation Science and Engineering* 15(1):45–56
- Moreels P, Perona P (2007) Evaluation of features detectors and descriptors based on 3d objects. *International journal of computer vision* 73(3):263–284
- Naimark L, Foxlin E (2002) Circular data matrix fiducial system and robust image processing for a wearable vision-inertial self-tracker. In: *Proceedings. International Symposium on Mixed and Augmented Reality, IEEE*, pp 27–36
- Pentenrieder K, Meier P, Klinker G, et al. (2006) Analysis of tracking accuracy for single-camera square-marker-based tracking. In: *Proc. Dritter Workshop Virtuelle und Erweiterte Realitt der GIFachgruppe VR/AR, Koblenz, Germany, Citeseer*
- Ri S, Hayashi S, Ogihara S, Tsuda H (2014) Accurate full-field optical displacement measurement technique using a digital camera and repeated patterns. *Optics Express* 22(8):9693–9706
- Sandoz P, Bonnans V, Gharbi T (2002) High-accuracy position and orientation measurement of extended two-dimensional surfaces by a phase-sensitive vision method. *Applied optics* 41(26):5503–5511
- Sattar J, Bourque E, Giguere P, Dudek G (2007) Fourier tags: Smoothly degradable fiducial markers for use in human-robot interaction. In: *Fourth Canadian Conference on Computer and Robot Vision (CRV'07), IEEE*, pp 165–174
- Shang W, Lu H, Wan W, Fukuda T, Shen Y (2016) Vision-based nano robotic system for high-throughput non-embedded cell cutting. *Scientific reports* 6(1):1–14
- Sugiura H, Sakuma S, Kaneko M, Arai F (2015) On-chip method to measure mechanical characteristics of a single cell by using moiré fringe. *Micromachines* 6(6):660–673
- Tamadazte B, Marchand E, Dembélé S, Le Fort-Piat N (2010) Cad model-based tracking and 3d visual-based control for mems microassembly. *The International Journal of Robotics Research* 29(11):1416–1434
- Yamahata C, Sarajlic E, Krijnen GJ, Gijs MA (2010) Subnanometer translation of microelectromechanical systems measured by discrete fourier analysis of ccd images. *Journal of Microelectromechanical Systems* 19(5):1273–1275
- Yao S, Li H, Pang S, Zhu B, Zhang X, Fatikow S (2021) A review of computer microvision-based precision motion measurement: Principles, characteristics, and applications. *IEEE Transactions on Instrumentation and Measurement* 70:1–28, DOI 10.1109/TIM.2021.3065436
- Zhong L, Zhang L (2019) A robust monocular 3d object tracking method combining statistical and photometric constraints. *International Journal of Computer Vision* 127(8):973–992